IVYSPRING INTERNATIONAL PUBLISHER

Theranostics

2018; 8(5): 1435-1448. doi: 10.7150/thno.22482

Research Paper

Targeted Delivery of Functionalized Upconversion Nanoparticles for Externally Triggered Photothermal/Photodynamic Therapies of Brain Glioblastoma

Yuan-Chung Tsai[1], Priya Vijayaraghavan[1], Wen-Hsuan Chiang[1], Hsin-Hung Chen[1,2], Te-I Liu[1], Ming-Yin Shen[1,3], Ayumu Omoto[4], Masao Kamimura[4,5], Kohei Soga[4,5]✉ and Hsin-Cheng Chiu[1]✉

1. Department of Biomedical Engineering and Environmental Sciences, National Tsing Hua University, Hsinchu 30013, Taiwan
2. Department of Chemical Engineering, National Chung Hsing University, Taichung 40249, Taiwan
3. Department of Surgery, National Taiwan University Hospital-Hsinchu Branch, Hsinchu 30013, Taiwan
4. Department of Materials Science and Technology, Tokyo University of Science, 6-3-1 Niijuku, Katsushika-ku, Tokyo 125-8585, Japan
5. Imaging Frontier Center (IFC), Research Institute for Science and Technology (RIST), Tokyo University of Science, 6-3-1 Niijuku, Katsushika-ku, Tokyo 125-8585, Japan

✉ Corresponding authors: Hsin-Cheng Chiu, Tel.: +886-35715131 ext 34233; Fax: 886-35718649; E-mail address : hscchiu@mx.nthu.edu.tw. Kohei Soga, Tel.: +81-3-5876-1717; Fax: 04-7124-1526; E-mail address: mail@ksoga.com.

Received: 2017.08.22; Accepted: 2017.12.05; Published: 2018.02.04

Abstract

Therapeutic efficacy of glioblastoma multiforme (GBM) is often severely limited by poor penetration of therapeutics through blood-brain barrier (BBB) into brain tissues and lack of tumor targeting. In this regard, a functionalized upconversion nanoparticle (UCNP)-based delivery system which can target brain tumor and convert deep tissue-penetrating near-infrared (NIR) light into visible light for precise phototherapies on brain tumor was developed in this work.

Methods: The UCNP-based phototherapy delivery system was acquired by assembly of oleic acid-coated UCNPs with angiopep-2/cholesterol-conjugated poly(ethylene glycol) and the hydrophobic photosensitizers. The hybrid nanoparticles (ANG-IMNPs) were characterized by DLS, TEM, UV/vis and fluorescence spectrophotometer. Cellular uptake was examined by laser scanning confocal microscopy and flow cytometry. The PDT/PTT effect of ANG-IMNPs was evaluated using MTT assay. Tumor accumulation of NPs was determined by a non-invasive *in vivo* imaging system (IVIS). The *in vivo* anti-glioma effect of ANG-IMNPs was evaluated by immunohistochemical (IHC) examination of tumor tissues and Kaplan-Meier survival analysis.

Results: *In vitro* data demonstrated enhanced uptake of ANG-IMNPs by murine astrocytoma cells (ALTS1C1) and pronounced cytotoxicity by combined NIR-triggered PDT and PTT. In consistence with the increased penetration of ANG-IMNPs through endothelial monolayer *in vitro*, the NPs have also shown significantly enhanced accumulation at brain tumor by IVIS. The IHC tissue examination confirmed prominent apoptotic and necrotic effects on tumor cells in mice receiving targeted dual photo-based therapies, which also led to enhanced median survival (24 days) as compared to the NP treatment without angiopep-2 (14 days).

Conclusion: *In vitro* and *in vivo* data strongly indicate that the ANG-IMNPs were capable of selectively delivering dual photosensitizers to brain astrocytoma tumors for effective PDT/PTT in conjugation with a substantially improved median survival. The therapeutic efficacy of ANG-IMNPs demonstrated in this study suggests their potential in overcoming BBB and establishing an effective treatment against GBM.

Key words: Upconversion nanoparticles, glioblastoma multiforme, orthotopic tumor, angiopep-2, photothermal therapy, photodynamic therapy

Introduction

Glioblastoma multiforme (GBM) is an extremely malignant brain tumor with poor prognosis and high mortality rates [1-3]. Although the current standard clinical treatments, including surgical resection, radiation, and chemotherapy, are effective to some extent, the median survival has not significantly improved and remains less than one year [4-6]. The intrinsic resistance of glioma cells to chemo- and radiotherapy along with the severe limitation of chemotherapy in penetrating through the blood-brain barrier (BBB) render the treatments less effective [7-9]. Furthermore, the highly migratory and invasive nature of a self-renewing subset of the heterogenic tumor cell population largely accounts for the high recurrence of glial tumors [10-13]. Despite great advances in neuroimaging, neurosurgery, and radiation and chemotherapy, the overall prognosis of GBM has not changed. There is thus a pressing need for improved GBM therapeutic strategies focusing on targeted and localized treatments. Besides exploiting the tumor-related enhanced permeation and retention (EPR) effects, selective delivery of nanomedicines to brain tumors has usually been achieved by targeting ligands, such as transferrin, cyclic arginine-glycine-aspartic acid (cRGD), and angiopep-2 [14-16]. Because of its dual targeting effects on endothelial and glioma cells, angiopep-2 is of great promise to enhance the accumulation of desired nanomedicines in brain tumors [17,18]. Xin et al. demonstrated enhanced nanoparticle (NP) accumulation in gliomas when angiopep-2 was conjugated on NP surfaces [19]. The effective penetration of the NPs across the BBB to tumor tissues was elicited by specific binding with low-density lipoprotein receptor-related protein-1 (LRP-1) receptor on endothelial cells, mediating the onset of receptor-mediated transcytosis [20].

Taking advantage of their localized treatment with reduced side effects, photo-induced therapies are alternative promising modalities for GBM treatment. Phototherapy involves strong light absorption by a photosensitizer to efficiently generate heat (photothermal therapy, PTT) or cytotoxic reactive oxygen species such as singlet O_2 (photodynamic therapy, PDT) [21,22]. For instance, Eldridge et al. have demonstrated the sound efficacy of PTT against GBM by near-infrared (NIR) irradiation of multiwalled carbon nanotubes in an *in vitro* tumor spheroid model [23]. Due to their innate tumor-tropic migration behavior, macrophages loaded with Au nanoshells have also been adopted for NIR-induced thermal ablation of GBM [24]. A delayed growth of GBM in rats receiving the cell-based photothermal therapy was observed compared to the untreated group. In spite of the extensive studies of nanoparticle-based PDT approaches against solid malignant tumors, PDT delivery via nanoconstructs to brain tumors and its therapeutic efficacy has been scarcely reported, probably because of the difficulty of NPs to cross the BBB and the limitation of light penetration required for photoactivation [25,26].

The application of PDT in solid tumor therapy is often impaired by the limited tissue penetration depth of UV/vis light, which is typically less than 2 mm [27-29]. Hence, to improve the therapeutic efficiency in intracranial tumors, the near-infrared (NIR) spectral window beyond 650 nm is better suited owing to its enhanced penetration, high tissue transparency, and minimal absorption by biological tissues. In this regard, lanthanide-doped upconversion nanoparticles (UCNPs), which can emit visible light upon 980 nm excitation, have been employed for transferring energy to organic photosensitizers through resonance energy transfer for improved phototherapy [30-33]. In a pioneering work by Idris et al., mesoporous silica-coated UCNPs as nano-transducers to convert deeply penetrating near-infrared to visible light were used to activate loaded dual-photosensitizers for effective PDT treatment of melanoma tumors [34]. Recently, Gd-doped UCNPs modified with angiopep-2-conjugated PEG were developed. Upon intravenous administration, there was a significant accumulation of NPs in tumors, enabling magnetic resonance/luminescence bimodal imaging for diagnosis of orthotopic glioblastoma [35].

In this study, a therapeutic strategy involving dual targetable UCNPs carrying both photothermal/photodynamic sensitizers was developed for the synergistic treatment of GBM. Conjugating UCNPs with PEG/angiopep-2 enables a GBM-specific co-delivery of the photothermal agent, IR-780, and photodynamic sensitizer, 5,10,15,20-tetrakis(3-hydroxyphenyl) chlorin (mTHPC), for externally triggered targeted therapy. Although IR-780 acting as a photodynamic agent has been reported elsewhere [36], the hyperthermia effect is more efficient under 808 nm irradiation [37,38]. Murine ALTS1C1 astrocytoma in C57BL/6J mice was employed as an orthotopic tumor model for evaluating the *in vivo* photothermal/photodynamic ablation of GBM. To the best of our knowledge, this is the first study demonstrating the combinational phototherapy in a hybrid functionalized NP system

for GBM treatment in an orthotopic model. The schematic in **Fig. 1** illustrates the delivery strategy of therapeutic nanoparticles developed herein for combinational phototherapy of orthotopic GBM.

Materials and Methods

Materials

Preparations of cholesterol-poly(ethylene glycol) (C-PEG) and cholesterol-poly(ethylene glycol)-maleimide (C-PEG-maleimide) were conducted as reported previously [39]. Ytterbium (III) nitrate pentahydrate ($Yb(NO_3)_3{\cdot}5H_2O$, 99.9%), erbium (III) nitrate pentahydrate ($Er(NO_3)_3{\cdot}5H_2O$, 99.9%), and IR-780 iodide were purchased from Sigma-Aldrich (USA). mTHPC was obtained from MedChem Express (Taiwan). Manganese (II) chloride tetrahydrate ($MnCl_2{\cdot}4H_2O$, 99.0%), sodium fluoride (NaF, 99.0%), oleic acid, and sodium hydroxide (NaOH, 97.0%) were acquired from Wako Pure Chemicals (Japan). Yttrium nitrate hexahydrate ($Y(NO_3)_3{\cdot}6H_2O$, 99.8%) was obtained from Kanto Chemicals (Japan). Angiopep-2 (TFFYGGSRGKRNNF KTEEYC) was synthesized by Neogene Medical Lab (Taiwan). Dulbecco's modified Eagle medium (DMEM), fetal bovine serum (FBS), and 0.25% trypsin–EDTA were obtained from Gibco (USA). 3-(4,5-Dimethylthiazol-2-yl)-2,5-diphenyltetrazolium bromide (MTT) was purchased from Sigma-Aldrich (USA). 4',6-Diamidino-2-phenylindole (DAPI), Alexa Fluor® 488, and anti-mouse caspase-3 antibody were supplied by Invitrogen (USA). ALTS1C1 (murine astrocytoma cells) were obtained through the courtesy of Dr. Chi-Shiun Chiang, Department of Biomedical Engineering and Environmental Sciences at National Tsing Hua University, Taiwan. ALTS1C1 cells were incubated at 37 °C in DMEM supplemented with 10% FBS under humidified 5% CO_2 atmosphere. C57BL/6JNarl male mice were purchased from the National Laboratory Animal Center, Taiwan. Approved guidelines for the care and use of laboratory animals by the Institutional Animal Care and Use Committee (IACUC: 10129) were followed throughout the study. Surgeries were performed under Zoletil-Rompun anesthesia, and all efforts were taken to minimize animal suffering [40].

Synthesis of UCNPs

Oleic acid-coated UCNPs were prepared by hydrothermal method [41]. NaOH (440 mg, 11 mmol), EtOH (7 mL), oleic acid (14 mL) and deionized water (2.2 mL) were mixed. $Y(NO_3)_3{\cdot}6H_2O$ (193 mg, 0.50 mmol), $Yb(NO_3)_3{\cdot}5H_2O$ (113 mg, 0.25 mmol), $Er(NO_3)_3{\cdot}6H_2O$ (12.4 mg, 0.028 mmol), and $MnCl_2$ (122 mg, 0.62 mmol) were added to the above solution under stirring. NaF (3 mL, 1.0 M) was then added dropwise to the mixture, and the solution was stirred for 20 min. The reaction mixture was then transferred into a polytetrafluoroethylene vessel and placed in a stainless-steel DAB-2 autoclave (Berghof GmbH, Germany) at 200 °C for 9 h under autogenous pressure. The resultant UCNPs were washed with ethanol, collected by centrifugation, and finally re-dispersed in cyclohexane.

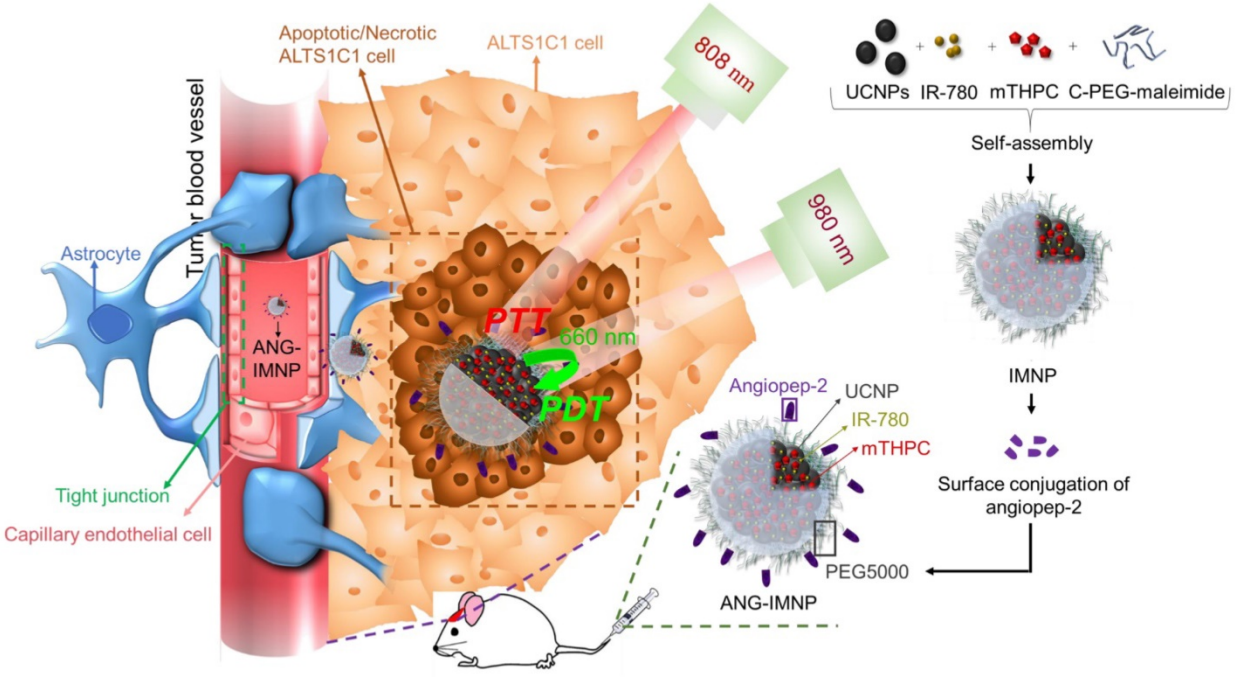

Figure 1. Illustration of active BBB penetration and the photothermal/photodynamic therapeutic design of ANG-IMNPs in an orthotopic glioblastoma tumor model.

Preparation and characterization of functionalized therapeutic NPs

The hybrid nano-assemblies loaded with IR-780 and mTHPC, denoted hereafter as IMNPs, were prepared by the nanoprecipitation technique. IR-780 (0.4 mg in 0.5 mL DMSO), mTHPC (0.4 mg in 0.5 mL DMSO), C-PEG-maleimide (2 mg in 0.1 mL $CHCl_3$), and UCNPs (2 mg in 0.1 mL cyclohexane) were mixed by ultrasonication for 10 min in an ice-water bath. Chloroform and cyclohexane were removed by rotary evaporation. The resulting solution was added dropwise into phosphate buffer (pH 7.4, ionic strength 0.01 M, 2.5 mL) under vigorous stirring. Unencapsulated IR-780 and mTHPC were removed by dialysis (Cellu Sep, MWCO 12-14 kDa) against phosphate buffer. Subsequently, angiopep-2 (0.12 mg) was added directly into the aqueous suspension of IMNPs and stirred at room temperature for 5 days. The final product, referred to hereafter as ANG-IMNPs, was purified by removing unreacted peptide species through dialysis against phosphate buffer. Light-induced physicochemical effects of ANG-IMNPs including light absorption, fluorescence emission, hyperthermia effect, and ROS generation were examined in comparison with free IR-780, mTHPC, C-PEG-coated UCNPs (pristine NPs), IR-780 loaded NPs (INPs), and mTHPC-loaded NPs (MNPs).

The mean hydrodynamic diameter (D_h), size distribution (polydispersity index, PDI), and zeta potential of ANG-IMNPs in the aqueous phase was determined by dynamic light scattering (DLS, ZetaSizer Nano Series, Malvern, U.K.). The morphology of UCNPs and ANG-IMNPs was examined by transmission electron microscopy (TEM, HT7700, Hitachi, Japan) operating at an accelerating voltage of 100 kV. X-ray diffraction (XRD) measurement of the NP samples was conducted on a TTRax III diffractometer (Rigaku, Japan). Energy dispersive X-ray (EDX) analysis was performed by field emission-scanning electron microscopy (FE-SEM, Hitachi S-4700 I, Japan). X-ray photoelectron spectra (XPS) were obtained by auger electron spectrometer (AES, PHI Quantera SXM/AES 650ULVAC-PHI) equipped with a hemispherical electron analyzer and a scanning monochromated AI Kα ($h\nu$ = 1486.6 eV) X-ray source. The encapsulation of the photosensitizers was examined from the absorption spectra of the NP solution in DMSO at 440 nm and 780 nm by a UV/vis spectrophotometer (U2900, Hitachi, Japan). The loading efficiency (L.E.) and content (L.C.) were calculated by the following equations:

L.E. (%) = (weight of drug loaded/weight of drug in feed) × 100%.

L.C. (%) = (weight of drug loaded/weight of drug-loaded NPs) × 100%.

Cellular uptake

The cellular uptake of NPs by ALTS1C1 cells was examined by laser scanning confocal microscopy (LSCM) and flow cytometry. ALTS1C1 cells at a density of 3 × 10^5 cells/well were seeded onto 22 mm round glass coverslips and cultured at 37 °C under 5% CO_2 overnight. The cells were then co-incubated with free mTHPC, IMNPs, ANG-IMNPs, and ANG-IMNPs together with free angiopep-2 as the blocking agent. After 4 h co-incubation, the coverslips were washed with PBS twice and immobilized with 4% paraformaldehyde. Cell nuclei were stained with DAPI (5 μg/mL). The cancer cells on coverslips were then fixed with mounting gel. The cellular images were visualized with a ZEISS LSM-780 equipped with two excitation lasers (DAPI, 405 nm; mTHPC, 633 nm). For flow cytometry analysis, ALTS1C1 cells (1.2 × 10^6 cells/well) were seeded in 6-well plates and treated with PBS (control), free mTHPC, IMNPs, ANG-IMNPs, and free angiopep-2/ANG-IMNPs in serum-free DMEM for 4 h at 37 °C. The cells were then trypsinized and resuspended in 500 μL of PBS. The mTHPC fluorescence intensity within the cells was analyzed by flow cytometry (FACSCalibur, BD Bioscience, USA).

In vitro photothermal and photodynamic effects of ANG-IMNPs

To evaluate the *in vitro* efficacy of PDT and PTT from the photoactivation of ANG-IMNPs against ALTS1C1 astrocytoma, ALTS1C1 cells (2 × 10^5 cells per well) were first seeded in 6-well plates and incubated in DMEM containing 10% FBS at 37 °C overnight. The cells were then co-incubated with ANG-IMNPs (IR-780: 10 μM; mTHPC: 12.9 μM) for an additional 4 h. After washing twice with PBS, cells were trypsinized and centrifuged. The cell pellet was resuspended in DMEM containing 10% FBS (20 μL), and the dispersion was illuminated for 5 min under different lasers (PTT: 808 nm laser, 0.36 W/cm^2; PDT: 980 nm laser, 0.8 W/cm^2). The laser-treated cells were reseeded in a 96-well plate and re-incubated for 24 h. The cell viability was examined by MTT assay with absorbance measurements at 570 nm using a micro plate reader (SpectraMax M5, Molecular Devices, USA). Free IR-780, mTHPC, and IMNPs, which lack angiopep-2 as the targeting ligand, at equivalent drug concentration were adopted as the control samples for comparison.

The *in vitro* photo-induced thermal effect of IR-780 either in free form or encapsulated within NPs on ALTS1C1 cells following laser irradiation at 808

nm (DPSSL DRIVER II, Taiwan) was examined using infrared thermal images from a digital thermographic camera (Thermoshot F20, NEC Avio Infrared Technologies, Germany). *In vitro* ROS generation by the photo-irradiation of ANG-IMNPs at 980 nm post cell co-incubation was evaluated by measurement of the fluorescence intensity (λ_{ex} = 504 nm; λ_{em} = 510-530 nm) of the singlet oxygen sensor green reagent (SOSG, 1.0 Invitrogen, USA) on a Hitachi F-7000 fluorescence spectrophotometer. The intracellular ROS level was examined by LSCM. ALTS1C1 cells (2×10^5 cells per well) were seeded in a 6-well plate and incubated at 37 °C overnight. The spent medium was then replaced with the medium containing free mTHPC, IMNPs or ANG-IMNPs for an additional 4 h. After washing with PBS, the cells were stained with SOSG (1.0 μM), and photo-irradiated (at either 660 nm or 980 nm laser) for 5 min. The intracellular SOSG emission was examined by LSCM.

In vitro BBB penetration of NPs

The *in vitro* BBB penetration efficiency of ANG-IMNPs was evaluated by transwell assay using a polycarbonate 24-well filter insert (1.0 μm pore size, BD Falcon) seeded with endothelial cells (bEnd.3 cell line) in a coherent monolayer [42,43]. The NPs were introduced into the insert, which was then accommodated in 24-well plates filled with DMEM. The content of yttrium in DMEM in the culture well at 24 h and 48 h was determined by inductively coupled plasma mass spectrometry (ICP-MS).

Orthotopic glioblastoma model and biodistribution

An orthotopic brain tumor model was established by implanting ALTS1C1 cells (5 x 10^7 cells/mL of F-12K medium) into mice intracranially. Male C57BL/6J mice (6-8 weeks old) were anesthetized with Zoletil-Rompun by intraperitoneal injection and placed in an animal stereotaxic apparatus (Stoelting, USA). The ALTS1C1 cells in F-12K medium (2 μL) were injected into the right striatum (1.8 mm lateral, 3 mm of depth) using a Hamilton syringe (10 μL) connected to the manipulator arm of the animal stereotaxic apparatus. After inoculation, the wound was sutured to avoid infection. Two weeks after tumor inoculation, NPs were intravenously administered into the tumor-bearing mice at an mTHPC dose of 1.4 mg/kg and/or IR-780 dose of 1.1 mg/kg. The time-evolved tumor accumulation of NPs post-injection was determined by the fluorescence signal of mTHPC (λ_{ex} = 675 nm, λ_{em} = 730-760 nm) using a non-invasive *in vivo* imaging system (Caliper IVIS Spectrum). Heart, liver, spleen, lung, kidney, and tumor were harvested for *ex vivo* optical imaging by IVIS.

Anti-GBM effect

Anti-GBM effect of ANG-IMNPs was analyzed by a Kaplan-Meier survival study. The tumor-bearing mice were treated with ANG-IMNPs, IMNPs, and the mixture of free IR-780 and mTHPC at an equivalent IR-780 dose of 1.1 mg/kg and mTHPC dose of 1.4 mg/kg through tail vein injection on day 14 post cancer cell inoculation. This was followed by laser irradiation at 808 nm (0.21 W/cm^2, 3 min) and/or 980 nm (0.5 W/cm^2, 10 min) 8 h post IV injection when applicable.

Immunohistochemical (IHC) examination of tumor tissues

The tumor-bearing mice received PDT and PTT in various formulations. The animals were then anesthetized and transcardially perfused with 4% paraformaldehyde in PBS using a 15-gauge needle through the cut ventricle into the ascending aorta. The brain was dissected from the mice and sliced into 7 μm thick sections. The slides were co-incubated with rabbit anti-mouse caspase-3 antibody at 4 °C. After 24 h, the slides were washed and incubated with the secondary antibody conjugated with Alexa Fluor 488 for 1 h at room temperature. The slides were stained with propidium iodide (PI) and visualized by LSCM. For histological examination, the tissue sections of major organs were H&E (hematoxylin and eosin) stained and studied under an optical microscope (Olympus IX70, Japan).

Results and Discussion

Synthesis and characterization of ANG-IMNPs

Yb- (18%) and Er (2%)-doped UCNPs were prepared by a hydrothermal synthetic procedure [41]. As shown in **Fig. 2A**, the TEM image of the UCNPs illustrates a cubic morphology. The representative SEM shows the shape and morphology of the UCNPs (**Fig. S1A**) and the corresponding SEM-EDX analysis of the inorganic NPs confirmed the presence of the basic elements Na, Y, Yb, and Er (**Fig. S1B**). The powder XRD pattern (**Fig. S1C**) of the UCNPs showed high crystallinity in the cubic phase structure of α-$NaYF_4$ (JCPDS: 06-0342). The UCNPs loaded with two phototherapeutic agents, IR-780 and mTHPC (IMNPs), were prepared via hydrophobic interactions of oleic acid-coated UCNPs, C-PEG-maleimide, and the hydrophobic photosensitizers. Covalent conjugation through the cysteine terminal of angiopep-2 onto the NP surfaces via the maleimide moieties of the PEG adducts conferred on the resulting NPs (ANG-IMNPs) the ability of BBB penetration and brain tumor targeting. The detailed

structural characterizations of IMNPs and ANG-IMNPs are illustrated in **Fig. 2**. The TEM images show the spherical morphology of each hybrid assembly of ANG-IMNPs (**Fig. 2B**). The hydrodynamic size of the NPs was characterized by DLS **(Fig. 2C)**. The ANG-IMNPs exhibited a mean hydrodynamic diameter of ~80 nm. To effectively penetrate through the BBB, nanomaterials of sizes less than 100 nm are highly desirable [44]. The ANG-IMNPs in this study exhibited an appropriate size to facilitate BBB penetration in conjunction with the aid of the peptide ligand. The successful chemical conjugation of angiopep-2 on IMNPs was further supported by XPS (**Fig. S1D**), which showed a binding energy of 160 eV representing the bonded thiol (–SH) group [45]. **Table 1** also shows that the mean size of IMNPs increased to 80±1 nm from 74±4 nm in diameter after conjugation with angiopep-2. The zeta potential measurements of IMNPs (-8.2±1.8 mV) and ANG-IMNPs (-4.7±0.8 mV) revealed nearly neutral charge at pH 7.4.

The optical properties of the NPs after being loaded with IR-780 and mTHPC, in terms of absorption and photoluminescence, were examined in comparison with free photosensitizers (**Fig. 2D,E**). The absorption spectrum of IMNPs showed the characteristic absorption peaks at 660 nm and 808 nm attributed to mTHPC and IR-780 species, respectively. The maximum absorption of free IR-780 in aqueous phase occurring at 780 nm apparently shifted to 808 nm when the photosensitizer was encapsulated within NPs by hydrophobic association. A similar red shift in the maximum absorption wavelength was also observed for free IR-780 in chloroform (**Fig. 2D**), obviously due to its residence in a nonpolar environment [46,47]. It is generally recognized that when the microenvironment of a photosensitizer switches from polar to nonpolar state, the energy gap between the excited and ground states can be reduced by the stabilization of the excited state rather than the ground state, leading to a red shift in wavelength of the maximum absorption [48]. **Fig. 2E** shows the photoluminescence spectra of the pristine NPs, INPs, MNPs, and IMNPs. Upon NIR excitation at 980 nm, the pristine NPs exhibited strong emission peaks at 540 nm and 660 nm. The inset in **Fig. 2E** is a photograph of the aqueous UCNP dispersion, illustrating strong upconverted luminescence in the visible region upon 980 nm excitation. In contrast to the pristine NPs and INPs, a significant decrease in the red emission at 660 nm occurred in the case of MNPs and IMNPs due to the resonance energy transfer from UCNPs to mTHPC [49,50]. The visible light at 660 nm produced by the upconversion of the NIR energy at 980 nm was obviously adopted by mTHPC for further ROS generation required in the PDT application as shown below. Strong hydrophobic interactions of both photosensitizers with the oleic acid residues on the UCNP surfaces and the cholesterol moieties of C-PEG adducts ensured the high loading efficiency (L.E.) and loading content (L.C.) for both IR-780 and mTHPC (L.E. = 98.0%, 96.0% and L.C. = 8.1%, 7.8%) in both IMNPs and ANG-IMNPs evaluated by the UV/vis measurements (**Table 1**). Limited premature leakage of the photosensitizers over a 48 h period, particularly the mTHPC species, from ANG-IMNPs was observed, implying the relatively stable confinement of the photoactive agents within the polymer/UCNP hybrid assemblies (**Fig. S2**).

The aqueous photostability of IR-780 and mTHPC from IMNPs in PBS was evaluated over a 96 h period by UV/vis measurements. The results are shown in **Fig. S3**. It is evident from the spectra that the absorbance of free IR-780 (**Fig. S3a**) and mTHPC (**Fig. S3B**) decreased considerably with time, whereas the change in the absorbance of both IR-780 and mTHPC was significantly alleviated when the photosensitizers were encapsulated (**Fig. S3C**). The increased photostability of both photosensitizers suggests their effective encapsulation within the NP hydrophobic cores, protecting them from self-aggregation and photo-bleaching. By contrast, the rapid degradation of free photosensitizers occurred due to their unstable photochemical properties under physiological conditions at 37 °C. The ANG-IMNPs also showed excellent colloidal stability over the 96 h period in different aqueous milieus because of the steric repulsion of the PEG chain segments on the NP surfaces (**Fig. S4**).

The photothermal and photodynamic effects of ANG-IMNPs were first demonstrated by individual NIR activations of IR-780 and mTHPC at 808 nm and 980 nm, respectively (**Fig. 3**). The temperature profiles of pristine NPs, free IR-780, ANG-INPs, and ANG-IMNPs by NIR irradiation at 808 nm over 5 min are shown in **Fig. 3A**. ANG-IMNPs and ANG-INPs demonstrated a rapid rise in temperature from 28 °C to 48 °C as compared to only a temperature increase of 3 °C for free IR-780. This is largely because of the red shift in light absorption of IR-780 embedded in the hybrid matrix, leading to the enhanced activation with the NIR laser at 808 nm. As expected, PBS and pristine NPs only showed a slight rise in temperature, confirming the generation of the photothermal effect exclusively from NIR irradiation of the IR-780 species within the NPs. The IR thermal images illustrated in **Fig. 3B** provide visual evidence of the photo-induced hyperthermia of IR-780-loaded hybrid NPs.

Table 1. DLS and drug loading characterization of IMNPs and ANG-IMNPs

Sample	D_h (nm)[a]	PDI[b]	Loading efficiency		Loading content		ζ-potential (mV)
			IR-780	mTHPC	IR-780	mTHPC	
IMNPs	74±4	0.14	78.0%	98.0%	6.5%	8.1%	-8.2±1.8
ANG-IMNPs	80±1	0.15	73.2%	96.0%	5.9%	7.8%	-4.7±0.8

[a]Hydrodynamic particle size (nm). [b]Polydispersity index.

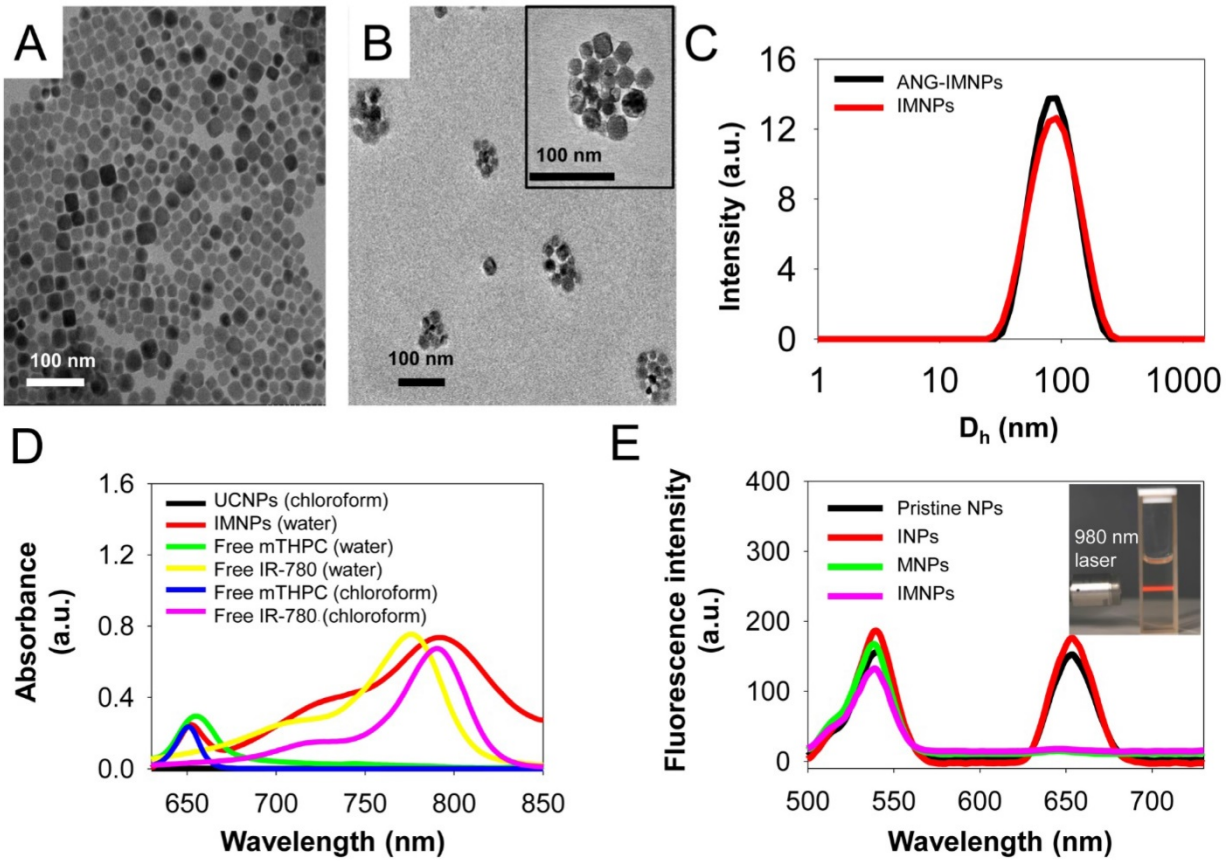

Figure 2. (A) TEM images of UCNPs, and **(B)** of ANG-IMNPs. The TEM image of a single ANG-IMNP is included in the inset. Scale bar: 100 nm. **(C)** The DLS size distribution profiles of IMNPs and ANG-IMNPs in PBS. **(D)** The UV/vis absorption spectra of UCNPs, IMNPs, free IR-780, and mTHPC in water and chloroform. **(E)** The fluorescence emission spectra of pristine NPs, INPs, MNPs, and IMNPs (λ_{ex} = 980 nm). The inset is a white-light photograph of the aqueous UCNPs dispersion upon 980 nm excitation using a 2 W diode laser.

The efficiency of ANG-IMNP to serve as a PDT agent by generating singlet oxygen was evaluated by the fluorescence intensity measurement of singlet oxygen sensor green (SOSG) at 525 nm. **Fig. 3C,D** illustrate SOSG fluorescence intensity as a quantitative measure of the ROS generation from various mTHPC-containing samples following NIR irradiation at 980 nm and 660 nm. Light absorption at a wavelength of ~660 nm is a prerequisite for mTHPC to generate ROS. However, the 660 nm laser could not be used due to its severely limited skull penetration (**Fig. S5**). Instead, the NIR laser at 980 nm with enhanced tissue penetration was adopted for its ability of *in situ* upconversion via UCNPs to generate 660 nm light (**Fig. 2E**). The fluorescence intensity of SOSG for ANG-IMNPs was substantially enhanced in comparison with free mTHPC upon 980 nm irradiation. It is noteworthy that the mixture of UCNPs with mTHPC gave rise to reduced SOSG fluorescence (i.e., ROS generation) compared to ANG-IMNPs, most probably due to the spatial separation of the UCNPs from mTHPC. Parallel experiments were also conducted to assess the efficiency of singlet oxygen generation of free mTHPC and ANG-IMNPs post 660 nm laser irradiation. The results, as displayed in **Fig. 3D**, confirmed ROS generation both from free mTHPC and ANG-IMNPs upon direct exposure to the laser light at 660 nm.

In vitro photo-induced therapy

Before *in vitro* evaluation of the photothermal/photodynamic therapeutic efficacy against astrocytoma ALTS1C1 cells, ANG-IMNPs were examined for their cellular uptake and BBB

penetration. The results of cellular uptake of ANG-IMNPs by LSCM and flow cytometric measurements are shown in **Fig. 4A** and **Fig. 4B**, respectively. The intracellular fluorescence level from the mTHPC species of ANG-IMNPs, particularly in the cytoplasm, was significantly enhanced in comparison with IMNPs and free mTHPC (**Fig. 4A** and **Fig. S6**). Furthermore, pretreatment of the cells with free angiopep-2 as a blocking agent considerably reduced the cellular uptake of ANG-IMNPs due to their competitive binding with the LRP-1 receptor on ALTS1C1 cells, confirming the important role of angiopep-2 in the entry pathway of ANG-decorated NPs into the cancer cells. Consistent with the LSCM measurements, the flow cytometry analysis also revealed the enhanced cellular uptake of angiopep-2-conjugated NPs while the cellular internalization of ANG-IMNPs was reduced by blocking the LRP-1 receptor with free angiopep-2 [51]. Owing to their nonpolar nature and severely limited solubility in aqueous medium, the cellular uptake of free mTHPC by ALTS1C1 cells was somewhat restricted. The penetration efficiency of ANG-IMNPs through the BBB was demonstrated by the *in vitro* transwell assay [39,40]. As shown in **Fig. 4C**, the conjugation of the NPs with the peptide ligand appreciably enhanced the fraction penetrating through the endothelial monolayer compared with IMNPs. It is well recognized that the angiopep-2 conjugation can facilitate the receptor-mediated transcytosis pathway to promote NP penetration through the endothelial monolayer [52,53]. The enhanced BBB penetration and cellular uptake confirmed that the ANG-IMNPs developed in this study exhibited an excellent targeting ability for glioblastoma.

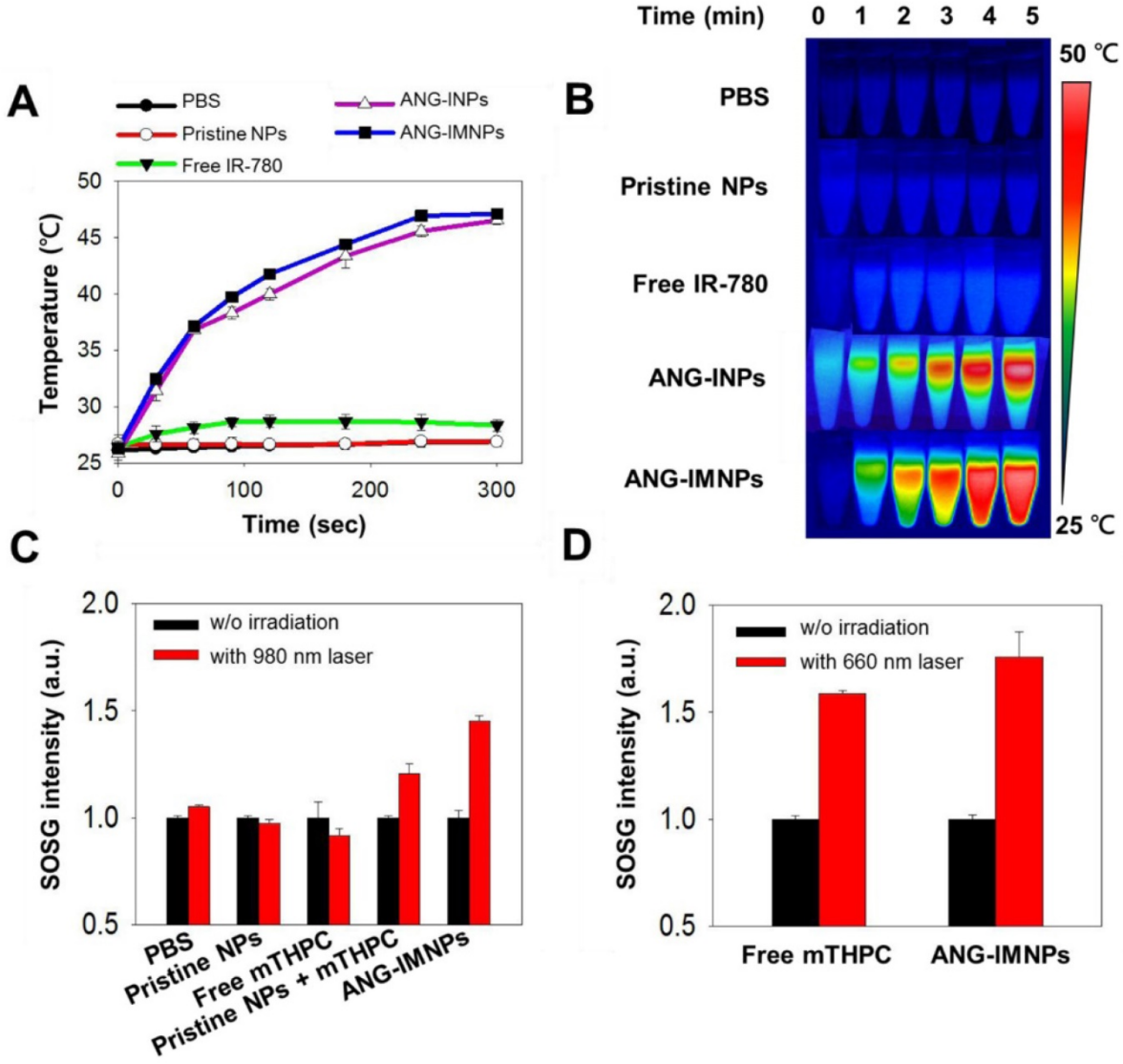

Figure 3. (A) Temperature elevation profiles and **(B)** thermal images of pristine NPs, free IR-780, ANG-INPs, and ANG-IMNPs in PBS with 808 nm NIR laser irradiation (1.0 W/cm^2, 5 min). **(C)** ROS generation in terms of the fluorescence intensity of SOSG from pristine NPs, free mTHPC, mixture of pristine NPs with mTHPC and ANG-IMNPs under 980 nm laser irradiation (0.75 W/cm^2, 20 s). **(D)** ROS generation by laser irradiation of free mTHPC and ANG-IMNPs at 660 nm (1.0 W/cm^2, 20 s).

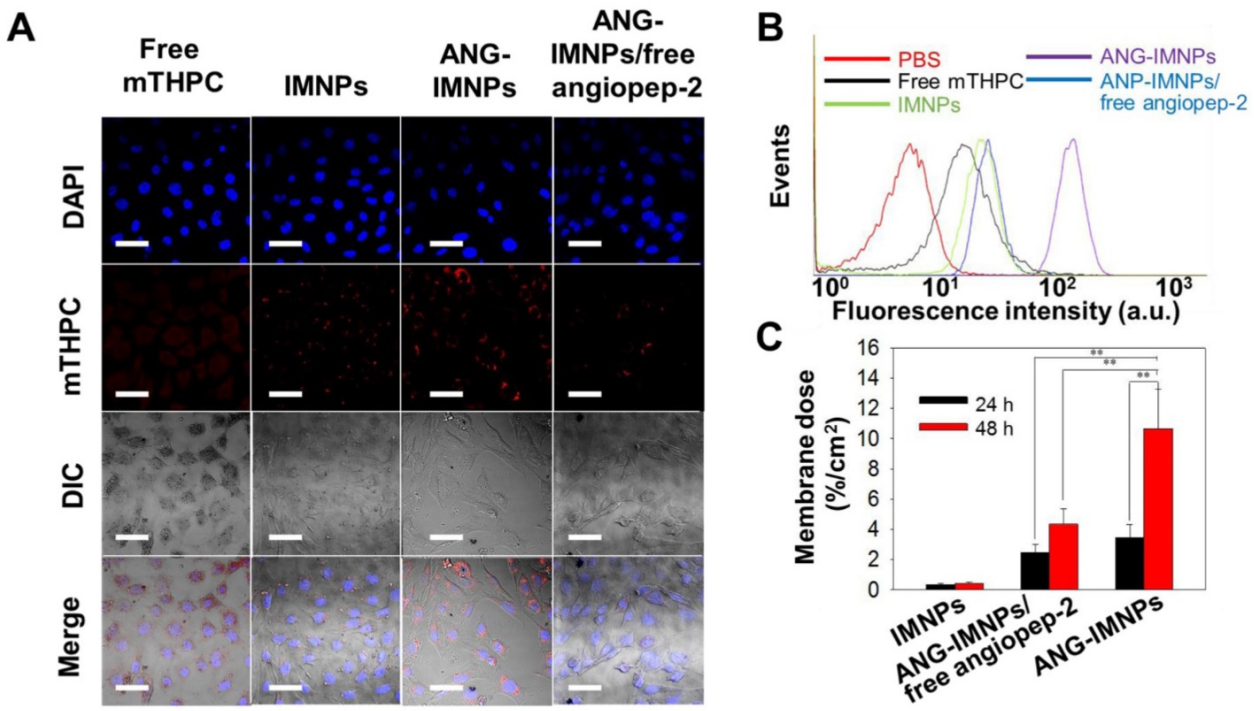

Figure 4. (A) LSCM images of the *in vitro* cellular uptake of free mTHPC, IMNPs, ANG-IMNPs, and ANG-IMNPs/free angiopep-2 by ALTS1C1 cells. Cell nuclei were stained with DAPI (λ_{ex} = 405 nm, λ_{em} = 450-500 nm) and uptake was monitored from the fluorescence channel for mTHPC (λ_{ex} = 633 nm, λ_{em} = 640-670 nm). Scale bar: 50 μm. **(B)** Flow cytometric histograms of ALTS1C1 cells after co-incubation with various mTHPC-containing samples for 4 h. **(C)** Fraction of IMNPs, ANG-IMNPs/free angiopep-2, and ANG-IMNPs that penetrated through the monolayer of bEnd.3 endothelial cells in the transwell-insert system. Basolateral medium was collected and analyzed at 24 h and 48 h by ICP-MS. Symbols and error bars are mean ± S.D. **P < 0.01.

The *in vitro* anticancer effect of ANG-IMNPs was further evaluated in ALTSICI cells using MTT assay. Under dark conditions, neither pristine NPs nor ANG-IMNPs induced noticeable cytotoxicity (**Fig. S7A**). Furthermore, laser irradiation at either 808 nm or 980 nm was harmless to the cells (**Fig. S7B**). As displayed in **Fig. 5A**, the viability of ALTS1C1 cells incubated with IMNPs and ANG-IMNPs receiving photodynamic or photothermal treatment reduced appreciably. By contrast, the survival of the cells treated with free photosensitizer together with the photo-irradiation at 808 nm or 980 nm remained high due to the lack of 660 nm irradiation directly or by upconversion reaction. **Fig. 5B** further demonstrates the strong ablation effect of the multimodal approach against the cancer cells (~82% cell death) compared with only ~35 % and 55% reduction, respectively, after receiving photothermal or photodynamic treatment alone. The results strongly suggest the superior cytotoxic effects against the astrocytoma cells by the combined photo-induced hyperthermia and singlet oxygen species of ANG-IMNPs. The NIR-activated hyperthermia in ALTS1C1 cells pretreated with either free IR-780 or ANG-IMNPs was further examined. **Fig. 5C,D** demonstrate the photothermal performance of IR-780 and ANG-IMNPs engulfed by the cancer cells upon exposure to 980/808 nm laser. With the 808 nm irradiation, the temperature of the ANG-IMNP-pretreated cells was significantly increased to ~43 °C compared to only 35 °C for free IR-780 due to the red shift effect in the absorption of IR-780 while being hydrophobically entrapped in NPs. The temperature of the cells untreated or treated with ANG-IMNPs receiving the 980 nm laser irradiation was raised to ~30 °C. This effect is ascribed mainly to the NIR absorption of water molecules at 980 nm. The NIR-induced ROS generation in ALTS1C1 cells was also examined by treating the cells with free mTHPC or ANG-IMNPs using SOSG as the fluorescence probe. As shown in **Fig. 5E**, the cells treated only with 660/980 nm laser irradiation exhibited poor ROS fluorescence signal. In contrast, the fluorescence signal intensity was enhanced upon exposure of the cells containing either free mTHPC or ANG-IMNPs to 660 nm laser. More importantly, the fluorescence signal of the ANG-IMNP-engulfed cancer cells irradiated at 980 nm was also increased as compared to the free mTHPC group with 980 nm irradiation. In agreement with the data shown in **Fig. 3**, the generation of 660 nm light via the upconversion reaction of the 980 nm NIR laser occurring inside the cancer cells induced intracellular ROS production, leading to appreciably enhanced fluorescence intensity (**Fig. 5E**) and reduced cell viability (**Fig. 5A**).

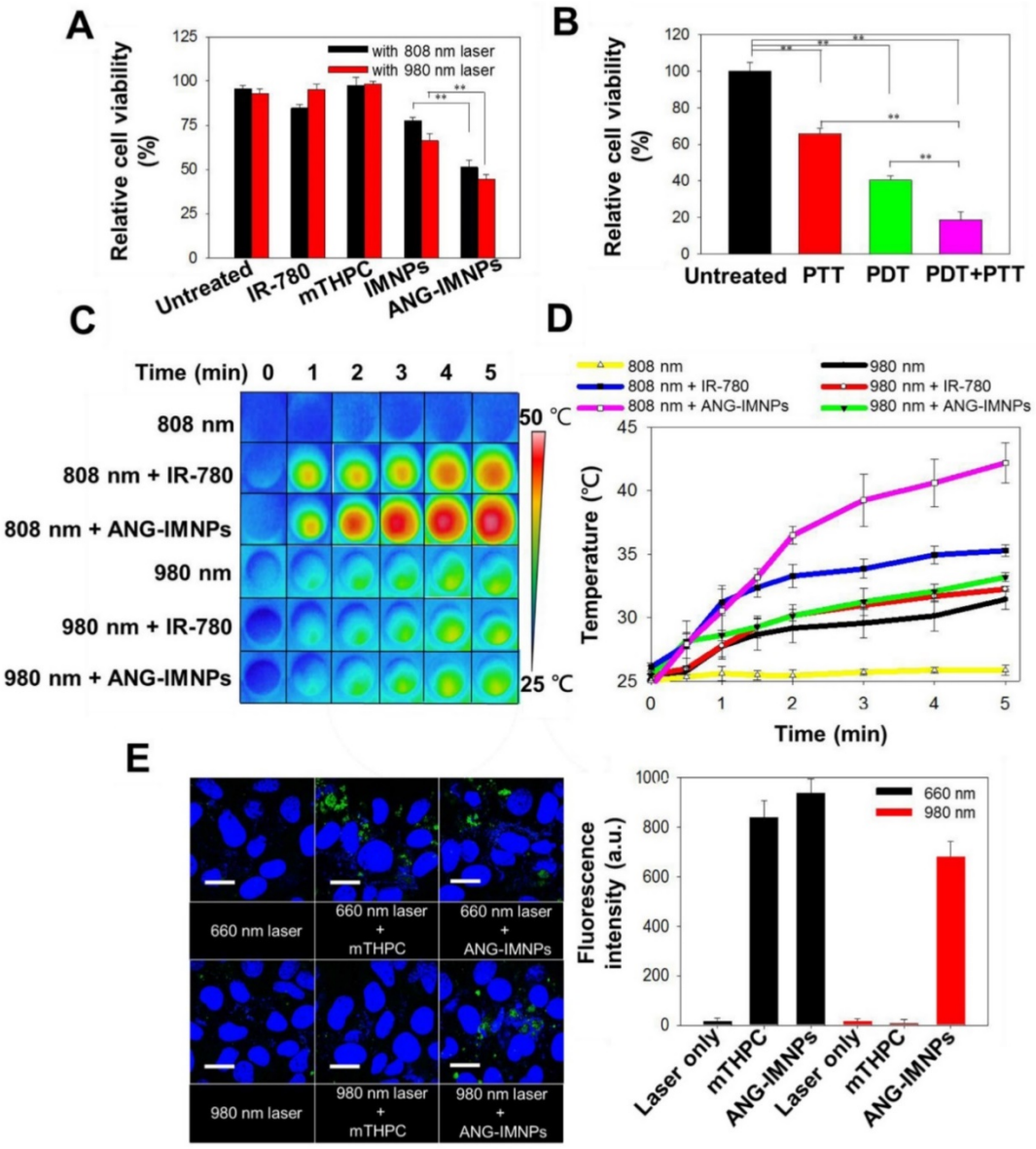

Figure 5. ***In vitro*** **PDT/PTT effects on ALTS1C1 cells. (A)** Cytotoxicity of free IR-780, mTHPC, IMNPs, and ANG-IMNPs under either 808 nm or 980 nm NIR irradiation. **(B)** Cytotoxicity of the PTT, PDT, and combinatorial therapies from ANG-IMNPs. Symbols and error bars are mean ± S.D. **P < 0.01. **(C)** Thermal images and **(D)** temperature elevation profiles of ALTS1C1 cells pretreated with IR-780 or ANG-IMNPs followed by 980/808 nm laser irradiation **(E)** LSCM images and the corresponding quantitative comparison of the *in vitro* ROS generation by SOSG staining shown in green in the ALTS1C1 cells post 660/980 nm light irradiation. Cell nuclei were stained with DAPI shown in blue. Scale bar: 20 μm.

In vivo imaging and biodistribution

Before demonstrating the *in vivo* therapeutic efficacy, the ANG-IMNPs were examined for tumor-targeting in C57BL/6J male mice bearing orthotopic brain tumors by IVIS. The images in **Fig. 6A** illustrate the considerable enhancement of mTHPC fluorescence signals at tumor sites in the mice at 2, 4, and 8 h post intravenous administration of ANG-IMNPs. The orthotopic tumors from the ANG-IMNP group exhibited much higher fluorescence signals compared to those treated with free mTHPC or IMNPs apparently because of the targeting effect of angiopep-2 conjugated on the NP surfaces. Despite the inherent passive accumulation of NPs at the tumor site by the EPR effect, the tumors treated with IMNPs in the absence of the angiopep-2 conjugation showed limited accumulation, most likely due to the restricted penetration of the NPs through the BBB. The *ex vivo* fluorescence signals of brain and other vital organs including heart, liver, spleen, lung, and kidney were also quantitatively evaluated at 8 h post administration (**Fig. 6B-E**). The results clearly indicate the significantly increased accumulation of ANG-IMNPs in the brain tumor compared to other formulations. In conjunction with the targeting peptide, the steric repulsion effects of surface PEGylation reduced clearance by major organs (liver

and spleen), thus prolonging NP circulation time and also facilitating tumor accumulation of ANG-IMNPs. By contrast, free mTHPC was found largely in the liver, the major organ responsible for its metabolism, along with only a small fraction in the brain. The fluorescence intensity of individual organs was further quantified and is displayed in **Fig. 6C**. A small molecule drug such as mTHPC with a nonpolar nature may cross the BBB by transmembrane diffusion [54]. The accumulation of intraperitoneally injected mTHPC in brain tumor has been reported elsewhere [55]. The enhanced targeting of the angiopep-2-conjugated ANG-IMNPs due to their specific binding to LRP-1 receptors on cell membranes of astrocytoma is further supported by the increased accessibility of ANG-IMNPs but not the IMNPs to the brain tumor (**Fig. 6D**). The quantitative evaluation of the brain accumulation of three different mTHPC-containing formulations is shown in **Fig. 6E**. The results demonstrated that ANG-IMNPs have prominently enhanced BBB penetration and tumor accumulation.

Photo-mediated destruction of orthotopic glioblastoma

Photo-induced cell apoptosis and necrosis of tumor tissues following the treatment of photodynamic therapy, photothermal therapy or combination were examined by caspase-3 marker and PI staining. **Fig. 7A** demonstrates that the signal of the caspase-3 protein, serving as an indicator for the apoptotic pathway, was prominently identified in tumor tissues of the mice treated with ANG-IMNPs and 980 nm irradiation [56,57]. By contrast, the hyperthermia ablation induced upon 808 nm irradiation resulted largely in necrosis, as indicated by prominent PI fluorescence signal from the stained tissues [58,59]. Both cell apoptosis and necrosis were observed following the *in vivo* combinatorial hyperthermia and photodynamic therapy against the brain tumor. On the other hand, tumor tissues treated with either the free photosensitizers or the IMNPs and the subsequent 980/808 nm irradiation showed a rather limited PI fluorescence signal and very weak, if any, caspase-3 protein expression. The limited efficacy is most probably because of the poor BBB penetration and tumor uptake of the combined therapy either in free drug form or encapsulated in IMNPs without the targeting peptide. The absence of the apoptotic effect for photodynamic therapy when treated in combination with free mTHPC and IR-780 (**Fig. 7A**) was expected because of the lack of the upconversion reaction from 980 nm laser to 660 nm light. The reason that the necrosis is the major cause of cell death from the IMNP treatment and 980/808 nm irradiation remains unclear. It is possible that the photodynamic therapy is somewhat impaired by the spatial factor between the released mTHPC and UCNPs.

The *in vivo* anti-glioma effect of ANG-IMNPs was evaluated by Kaplan-Meier survival analysis. Mice receiving different treatments were monitored daily over 28 days (**Fig. 7B**). Following the ANG-IMNP treatment, the median survival of the mice subjected to combinatorial 980/808 nm laser irradiation was appreciably extended to 24 days compared to only 14 days in the group receiving IMNPs + 980/808 nm, 18 days with ANG-IMNPs + 808 nm and 16 days with ANG-IMNPs + 980 nm irradiation. Because of the inherent aggressive progression behavior of ALTS1C1 astrocytoma cells in brain tumors, the median survival was rather short, merely 8 days for the PBS group and 14 days following the ANG-IMNP treatment in the absence of irradiation. In the latter group, the extension in life span was caused largely by the chemotherapy effect of IR-780 [60,61]. No significant change in body weight of mice over time with varying treatments was observed, suggesting that the combinatorial phototherapy does not elicit severe side effects (**Fig. S8**). The *in vivo* systemic toxicity of varying formulations was examined with tissue H&E staining (**Fig. S9**). Consistent with the body weight data, neither inflammatory infiltrates nor pathological changes were observed in the ANG-IMNPs-treated mice compared to the PBS control group. This is probably because of the reduced NP uptake by the major organs due to surface PEGylation and the localized activation of the combinational therapy on GBM.

Conclusions

In this study, we developed organic/UCNP hybrid nanoassemblies (ANG-IMNPs) loaded with IR-780/mTHPC and decorated with C-PEG-ANG by anchoring the cholesterol moieties into the NP hydrophobic regions. The hybrid nanoparticles were capable of selectively delivering dual photosensitizers to brain astrocytoma tumors for combined photothermal/photodynamic therapy. The *in vitro* evaluation of cellular uptake and cytotoxicity against ALTS1C1 astrocytoma cells suggest that ANG-IMNPs can be efficiently internalized by the cancer cells with successful combinational therapeutic effects of ~80% cytotoxicity. The *in vivo* biodistribution studies showed enhanced accumulation of ANG-IMNPs at the tumor site due to the targeted tumor delivery by angiopep-2. The *in vivo* photoactivated dual therapies caused extensive apoptosis and necrosis of brain tumors receiving ANG-IMNPs. The median survival of the orthotopic tumor-bearing mice was prolonged

to 24 days compared to only 14 days for the therapeutic nanoparticles without angiopep-2 conjugation. The therapeutic efficacy of ANG-IMNPs demonstrated in this study suggest their potential in overcoming BBB and establishing an effective treatment against GBM.

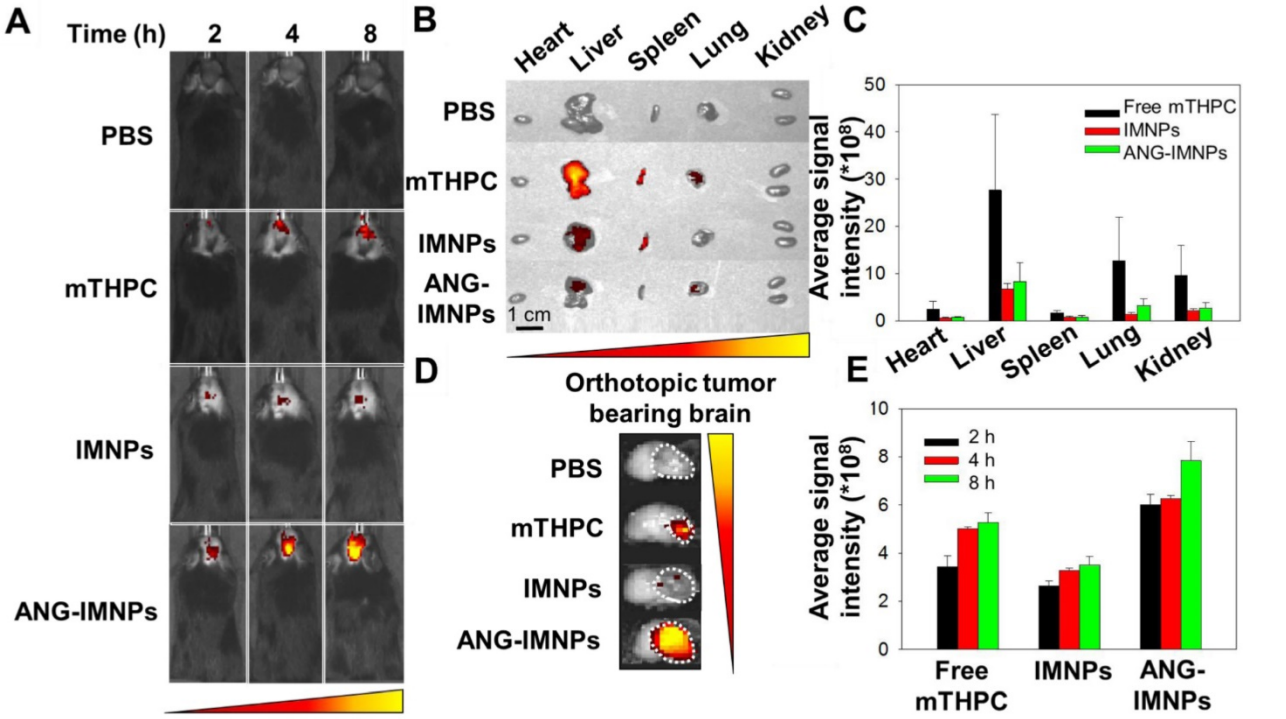

Figure 6. (A) *In vivo* fluorescence images of glioma-bearing mice intravenously receiving different mTHPC-containing formulations. **(B)** *Ex vivo* fluorescence images of major organs. **(C)** Average mTHPC fluorescence intensity in major organs. **(D)** *Ex vivo* fluorescence images of the brain tumor and **(E)** quantitative evaluation of the tumor accumulation. The organs and brain tumor were isolated 8 h post intravenous administration.

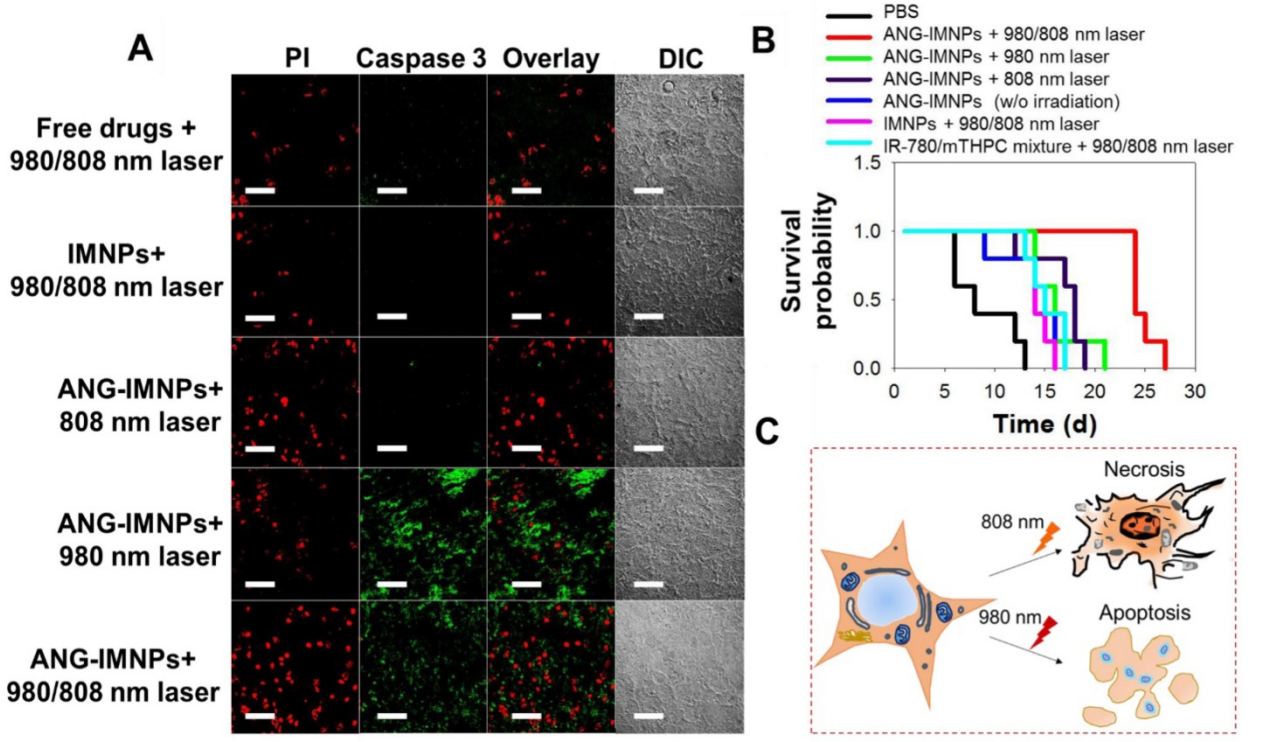

Figure 7. (A) Fluorescence images of tumor tissue sections from the tumor-bearing mice treated with different formulations. Cell death was identified with caspase-3 marker (apoptosis) and PI (late apoptosis and necrosis). Scale bar: 50 μm. **(B)** Kaplan-Meier survival curves of the glioma-bearing mice (n = 5). **(C)** A schematic of the cancer cell necrosis and apoptosis by ANG-IMNPs with 980/808 nm laser irradiation.

Abbreviations

GBM: glioblastoma multiforme; BBB: blood-brain barrier; UCNP: upconversion nanoparticle; INPs: IR-780 loaded nanoparticles; MNPs: mTHPC-loaded nanoparticles; IMNPs: IR-780/mTHPC loaded nanoparticles; ANG-IMNPs: angiopep-2 decorated IR-780/mTHPC loaded nanoparticles; PTT: photothermal therapy; PDT: photodynamic therapy; mTHPC: 5,10,15,20-tetrakis(3-hydroxyphenyl) chlorin; EPR: enhanced permeation and retention; cRGD: cyclic arginine-glycine-aspartic acid; NP: nanoparticle; LRP-1: low-density lipoprotein receptor-related protein-1; NIR: near-infrared; C-PEG: cholesterol-poly(ethylene glycol); DMEM: Dulbecco's modified Eagle medium; PBS: phosphate buffer saline; FBS: fetal bovine serum; MTT: 3-(4,5-Dimethylthiazol-2-yl)-2,5-diphenyltetrazolium bromide; DAPI: 4',6-Diamidino-2-phenylindole; IACUC: institutional animal care and use committee; D_h: mean hydrodynamic diameter; PDI: polydispersity index; DLS: dynamic light scattering; TEM: transmission electron microscopy; XRD: X-ray diffraction; EDX: energy dispersive X-ray; FE-SEM: field emission-scanning electron microscopy; XPS: X-ray photoelectron spectra; AES: auger electron spectrometer; LSCM: laser scanning confocal microscopy; SOSG: singlet oxygen sensor green; ICP-MS: inductively coupled plasma mass spectrometry; IVIS: *in vivo* imaging system; H&E: hematoxylin and eosin; PI: propidium iodide; ROS: reactive oxygen species; IHC: immunohistochemical.

Acknowledgments

This work is supported by the Ministry of Science and Technology, Taiwan (MOST 105-2627-M-007-007- and MOST 105-2221-E-007-043-MY3) and the National Tsing Hua University, Taiwan (106N522CE1).

Supplementary Material

Supplementary figures.
http://www.thno.org/v08p1435s1.pdf

Competing Interests

The authors have declared that no competing interest exists.

References

1. Stupp R, Mason WP, van den Bent MJ, et al. Radiotherapy plus concomitant and adjuvant temozolomide for glioblastoma. N Engl J Med. 2005; 352: 987-996.
2. Parsons DW, Jones S, Zhang X, et al. An integrated genomic analysis of human glioblastoma multiforme. Science. 2008; 321: 1807-1812.
3. Walid MS. Prognostic factors for long-term survival after glioblastoma. Perm J. 2008; 12: 45-48.
4. Ostrom QT, Gittleman H, Farah P, et al. CBTRUS statistical report: primary brain and central nervous system tumors diagnosed in the United States in 2006-2010. Neuro Oncol. 2013; 15: 1-56.
5. Brandes AA. State-of-the-art treatment of high-grade brain tumors. Semin Oncol. 2003; 30: 4-9.
6. Chen H, Ward MH, Tucker KL, et al. Diet and risk of adult glioma in eastern Nebraska, United States. Cancer Causes Control. 2002; 13: 647-655.
7. Bao S, Wu Q, McLendon RE, et al. Glioma stem cells promote radioresistance by preferential activation of the DNA damage response. Nature. 2006; 444: 756-760.
8. Mannino M, Gomez-Roman N, Hochegger H, et al. Differential sensitivity of glioma stem cells to Aurora kinase A inhibitors: implications for stem cell mitosis and centrosome dynamics. Stem Cell Res. 2014; 13: 135-143.
9. Chen Y, Liu L. Modern methods for delivery of drugs across the blood-brain barrier. Adv Drug Deliv Rev. 2012; 64: 640-665.
10. Lim DA, Cha S, Mayo MC, et al. Relationship of glioblastoma multiforme to neural stem cell regions predicts invasive and multifocal tumor phenotype. Neuro Oncol. 2007; 4: 424-429.
11. Chen J, Li Y, Yu TS, et al. A restricted cell population propagates glioblastoma growth after chemotherapy. Nature. 2012; 488: 522-526.
12. Beier D, Schulz JB, Beier CP. Chemoresistance of glioblastoma cancer stem cells--much more complex than expected. Mol Cancer. 2011; 10: 128.
13. Roos A, Ding Z, Loftus JC, et al. Molecular and microenvironmental determinants of glioma stem-like cell survival and invasion. Front Oncol. 2017; 7: 120.
14. Blanco E, Shen H, Ferrari M. Principles of nanoparticle design for overcoming biological barriers to drug delivery. Nat Biotechnol. 2015; 33: 941-951.
15. Gormley AJ, Greish K, Ray A, et al. Gold nanorod mediated plasmonic photothermal therapy: a tool to enhance macromolecular delivery. Int J Pharm. 2011; 415: 315-318.
16. Dickerson EB, Dreaden EC, Huang XH, et al. Gold nanorod assisted near-infrared plasmonic photothermal therapy (PPTT) of squamous cell carcinoma in mice. Cancer Lett. 2008; 269: 57-66.
17. Huang XH, Jain PK, El-Sayed IH, et al. Plasmonic photothermal therapy (PPTT) using gold nanoparticles. Lasers Med Sci. 2008; 23: 217-228.
18. Liu YL, Gunda V, Zhu X, et al. Theranostic near-infrared fluorescent nanoplatform for imaging and systemic siRNA delivery to metastatic anaplastic thyroid cancer. Proc Natl Acad Sci USA. 2016; 113: 7750-7755.
19. Lu F, Pang Z, Zhao J, et al. Angiopep2-conjugated poly(ethylene glycol)-co-poly(ε-caprolactone)polymersomes for dual-targeting drug delivery to glioma in rats. Int J Nanomed. 2017; 12: 2117-2127.
20. Pourgholi F, Hajivalili M, Farhad JN, et al. Nanoparticles: novel vehicles in treatment of glioblastoma. Biomed Pharmacother. 2016; 77: 98-107.
21. Chatterjee DK, Fong LS, Zhang Y. Nanoparticles in photodynamic therapy: an emerging paradigm. Adv Drug Deliv Rev. 2008; 60: 1627-1637.
22. Huang XH, El-Sayed IH, Qian W, et al. Cancer cell imaging and photothermal therapy in the near-infrared region by using gold nanorods. J Am Chem Soc. 2006; 128: 2115-2120.
23. Eldridge BN, Bernish BW, Fahrenholtz CD, et al. Photothermal therapy of glioblastoma multiforme using multiwalled carbon nanotubes optimized for diffusion in extracellular space. ACS Biomater Sci Eng. 2016; 2: 963-976.
24. Hirschberg H, Madsen SJ. Cell mediated photothermal therapy of brain tumors. J Neuroimmune Pharmacol. 2017; 12: 99-106.
25. Huang N, Cheng S, Zhang X, et al. Efficacy of NGR peptide-modified PEGylated quantum dots for crossing the blood-brain barrier and targeted fluorescence imaging of glioma and tumor vasculature. Nanoed-Nanotechnol Biol Med. 2017; 13: 83-93.
26. Lee J, Lee TS, Ryu J, et al. RGD-peptide-conjugated multimodal $NaGdF_4$: Yb^{3+}/Er^{3+} nanophosphors for upconversion luminescence, MR, and PET imaging of tumor angiogenesis. J Nucl Med. 2013; 54: 96-103.
27. Hong GS, Diao S, Chang JL, et al. Through-skull fluorescence imaging of the brain in a new near-infrared window. Nat Photonics. 2014; 8: 723-730.
28. Wang M, Abbineni G, Clevenger A, et al. Upconversion nanoparticles: synthesis, surface modification and biological applications. Nanomed-Nanotechnol Biol Med. 2011; 7: 710-729.
29. Ntziachristos V, Bremer C, Weissleder R. Fluorescence imaging with near-infrared light: new technological advances that enable *in vivo* molecular imaging. Eur Radiol. 2003; 13: 195-208.
30. Kamimura M, Omoto A, Chiu HC, et al. Enhanced red upconversion emission of $NaYF_4$:Yb^{3+}, Er^{3+}, Mn^{2+} nanoparticles for near-infrared induced photodynamic therapy and fluorescence imaging. Chem Lett. 2017; 46: 1076-1078.
31. Wang C, Cheng L, Liu Z. Upconversion nanoparticles for photodynamic therapy and other cancer therapeutics. Theranostics. 2013; 3: 317-330.
32. Gai S, Li C, Yang P, et al. Recent progress in rare earth micro/nanocrystals: soft chemical synthesis, luminescent properties, and biomedical applications. Chem Rev. 2014; 114: 2343-2389.
33. Gai S, Yang P, Li X, et al. Monodisperse CeF_3, CeF_3:Tb^{3+}, and CeF_3:Tb^{3+}@LaF_3 core/shell nanocrystals: synthesis and luminescent properties. J Mater Chem. 2011; 21: 14610-14615.
34. Idris NM, Gnanasammandhan MK, Zhang J, et al. *In vivo* photodynamic therapy using upconversion nanoparticles as remote-controlled nanotransducers. Nat Med. 2012; 18: 1580–1585.

35. Ni D, Zhang J, Bu W, et al. Dual-targeting upconversion nanoprobes across the blood-brain barrier for magnetic resonance/fluorescence imaging of intracranial glioblastoma. ACS Nano. 2014; 8: 1231-1242.
36. Wang K, Zhang Y, Wang J, et al. Self-assembled IR780-loaded transferrin nanoparticles as an imaging, targeting and PDT/PTT agent for cancer therapy. Sci Rep. 2016; 6: 27421.
37. Yue C, Liu P, Zheng M, et al. IR-780 dye loaded tumor targeting theranostic nanoparticles for NIR imaging and photothermal therapy. Biomaterials. 2013; 34: 6853-6861.
38. Yuan A, Wu J, Tang X, et al. Application of near-infrared dyes for tumor imaging, photothermal, and photodynamic therapies. J Pharm Sci. 2013; 102: 6-28.
39. Chen HH, Huang WC, Chiang WH, et al. pH-Responsive therapeutic solid lipid nanoparticles for reducing P-glycoprotein-mediated drug efflux of multidrug resistant cancer cells. Int J Nanomed. 2015; 10: 5035-5048.
40. Huang WC, Chiang WH, Cheng YH, et al. Tumortropic monocyte-mediated delivery of echogenic polymer bubbles and therapeutic vesicles for chemotherapy of tumor hypoxia. Biomaterials. 2015; 71: 71-83.
41. He EJ, Zheng HR, Gao W, et al. Enhancement and regulation of fluorescence emission from $NaYF_4$:Yb^{3+}, Er^{3+} nanocrystals by codoping Mn^{2+} ions. J Nanosci Nanotechnol. 2014; 14: 4139-4146.
42. Gao H, Yang Z, Zhang S, et al. Study and evaluation of mechanisms of dual targeting drug delivery system with tumor microenvironment assays compared with normal assays. Acta Biomater. 2014; 10: 858-867.
43. Shi W, Cui X, Shi J, et al. Overcoming the blood-brain barrier for glioma-targeted therapy based on an interleukin-6 receptor-ediated micelle system. RSC Adv. 2017; 7: 27162-27169.
44. Barua S, Mitragotri S. Challenges associated with penetration of nanoparticles across cell and tissue barriers: a review of current status and future prospects. Nano Today. 2014; 9: 223-243.
45. McCormick H, McMillan R, Merrett K, et al. XPS study of the effect of the conditions of peptide chemisorption to gold and silver coated polymer surfaces. Colloid Surf B-Biointerfaces. 2002; 26: 351-363.
46. Jiang C, Cheng H, Yuan A, et al. Hydrophobic IR780 encapsulated in biodegradable human serum albumin nanoparticles for photothermal and photodynamic therapy. Acta Biomater. 2015; 14: 61-69.
47. Wang K, Zhang Y, Wang J, et al. Self-assembled IR780-loaded transferrin nanoparticles as an imaging, targeting and PDT/PTT agent for cancer therapy. Sci Rep. 2016; 6: 27421.
48. Reichardt C. Solyatochromic dyes as solvent polarity indicators. Chem Rev. 1994; 94: 2319-2358.
49. Wang X, Liu K, Yang GB, et al. Near-infrared light triggered photodynamic therapy in combination with gene therapy using upconversion nanoparticles for effective cancer cell killing. Nanoscale. 2014; 6: 9198-9205.
50. Li ZW, Wang C, Cheng L, et al. PEG-functionalized iron oxide nanoclusters loaded with chlorin e6 for targeted, NIR light induced, photodynamic therapy. Biomaterials. 2013; 34: 9160-9170.
51. Xin HL, Jiang XY, Gu JJ, et al. Angiopep-conjugated poly(ethyleneglycol)-co-poly(epsilon-caprolactone) nanoparticles as dual-targeting drug delivery system for brain glioma. Biomaterials. 2011; 32: 4293-4305.
52. Wei X, Zhan C, Chen X, et al. Retro-inverso isomer of angiopep-2: a stable d-peptide ligand inspires brain-targeted drug delivery. Mol Pharm. 2014; 11: 3261-3268.
53. Fang F, Zou D, Wang W, et al. Non-invasive approaches for drug delivery to the brain based on the receptor mediated transport. Mater Sci Eng C-Mater Biol Appl. 2017; 76: 1316-1327.
54. Banks WA. Characteristics of compounds that cross the blood-brain barrier. BMC Neurol. 2009; 9: 1-5.
55. Kostron H, Obwegeser A, Jakober R, et al. Experimental and clinical results of mTHPC (Foscan)-mediated photodynamic therapy for malignant brain tumors. Proc SPIE. 1998; 3247: 40-45.
56. Reidy K, Campanile C, Muff R, et al. mTHPC-mediated photodynamic therapy is effective in the metastatic human 143B osteosarcoma cells. Photochem Photobiol. 2012; 88: 721-727.
57. Wu Y, Xing D, Luo S, et al. Detection of caspase-3 activation in single cells by fluorescence resonance energy transfer during photodynamic therapy induced apoptosis. Cancer Lett. 2006; 235: 239-247.
58. Hung CC, Huang WC, Lin YW, et al. Active tumor permeation and uptake of surface charge-switchable theranostic nanoparticles for imaging-guided photothermal/chemo combinatiorial therapy. Theranostics. 2016; 6: 302-317.
59. Huang P, Rong P, Jin A, et al. Dye-loaded ferritin nanocages for multimodal imaging and photothermal therapy. Adv Mater. 2014; 26: 6401-6408.
60. Zhan Y, Cao X, Cao X, et al. Silica cross-linked micellar core-shell nanoparticles encapsulating IR-780 with strong bright and good biocompatibility for optical imaging *in vivo*. J Biomed Nanotechnol. 2017; 13: 144-154.
61. Wang Y, Liu T, Zhang E et al. Preferential accumulation of the near infrared heptamethine dye IR-780 in the mitochondria of drug-resistant lung cancer cells. Biomaterials. 2014; 35: 4116-4124.